

# The architecture of the mammalian respirasome

Jinke Gu<sup>1\*</sup>, Meng Wu<sup>1\*</sup>, Runyu Guo<sup>1\*</sup>, Kaige Yan<sup>1</sup>, Jianlin Lei<sup>1</sup>, Ning Gao<sup>1</sup> & Maojun Yang<sup>1</sup>

The respiratory chain complexes I, III and IV (CI, CIII and CIV) are present in the bacterial membrane or the inner mitochondrial membrane and have a role of transferring electrons and establishing the proton gradient for ATP synthesis by complex V. The respiratory chain complexes can assemble into supercomplexes (SCs), but their precise arrangement is unknown. Here we report a 5.4 Å cryo-electron microscopy structure of the major 1.7 megadalton  $\text{SCI}_1\text{III}_2\text{IV}_1$  respirasome purified from porcine heart. The CIII dimer and CIV bind at the same side of the L-shaped CI, with their transmembrane domains essentially aligned to form a transmembrane disk. Compared to free CI, the CI in the respirasome is more compact because of interactions with CIII and CIV. The NDUFA11 and NDUFB9 supernumerary subunits of CI contribute to the oligomerization of CI and CIII. The structure of the respirasome provides information on the precise arrangements of the respiratory chain complexes in mitochondria.

The mitochondrial respiratory chain complexes reside in the inner mitochondrial membrane or cristae and have important roles in energy conversion. Respiratory chain complexes consist of four multi-subunit complexes named complex I (NADH:ubiquinone oxidoreductase), complex II (succinate dehydrogenase), complex III (cytochrome *bc*<sub>1</sub> complex), and complex IV (cytochrome *c* oxidase). Three complexes (CI, CIII and CIV) collectively establish the proton gradient across the inner mitochondrial membrane for complex V (CV, ATP synthase) to synthesize ATP. The respiratory chain complexes and CV together form the oxidative phosphorylation (OXPHOS) system. Dysfunction of mitochondrial respiratory chain complexes generates reactive oxygen or nitrogen species, and this type of dysfunction is implicated in many human diseases<sup>1–3</sup>, including Alzheimer's and Parkinson's diseases, multiple sclerosis, Friedreich's ataxia and amyotrophic lateral sclerosis.

In addition to forming individual complexes that are randomly scattered in the membrane, much evidence suggests that these complexes can also be organized into defined, active super-structures<sup>4</sup>. The composition of supercomplexes can vary substantially<sup>5</sup>. Various forms of supercomplexes consisting of different numbers and types of individual complexes have been reported in different species. Supercomplexes purified from bacteria containing CIII and CIV had been overlooked for a long time<sup>6,7</sup> until a new electrophoresis strategy called blue native PAGE (BNPA) was developed for mitochondria research. High-molecular-weight bands observed during BNPA analyses of digitonin-solubilized preparations were found to contain stable compositions of individual complexes<sup>4,8</sup>. In *Saccharomyces cerevisiae*, which does not have the multi-subunit CI, stable supercomplexes containing  $\text{III}_2\text{IV}_1$  (750 kDa) and  $\text{III}_2\text{IV}_2$  (1,000 kDa) could be extracted<sup>9</sup>. In *Arabidopsis thaliana*, the main form of the supercomplex contains I<sub>1</sub>I<sub>2</sub>I<sub>2</sub>. In mammals, a  $\text{SCI}_1\text{III}_2\text{IV}_1$  was obtained from bovine heart<sup>10–13</sup>, whereas CII was also proposed to be involved in forming supercomplexes in mouse liver mitochondria<sup>14</sup>.

In bovine heart, after digitonin solubilization, ~80% of total CI is distributed into supercomplexes, whereas only ~20% of CI was found in the free form. Approximately two-thirds of total CIII was also found in various forms of supercomplexes, whereas the majority of CIV (~85%) was found in the free form<sup>4</sup>. These data suggest that respiratory chain

complexes might have a structural interdependence in mitochondria. Indeed, previous studies have demonstrated the assembled CIII (refs 15, 16) and CIV (ref. 17) are required to stabilize CI in mammalian cells.

In the respiratory chain, supercomplexes containing complexes I, III, and IV were proposed by a few groups to form respiratory strings, in which different supercomplex forms are arranged in an ordered linear pattern along the inner mitochondrial membrane cristae<sup>18–20</sup>, though our knowledge about this organization is rather limited. Among these supramolecular assembly states, the structure of  $\text{SCI}_1\text{III}_2\text{IV}_1$  generated great interest and was among the most intensively studied<sup>12,13,21,22</sup>. However, there had been a lack of precise interpretation of inter-complex interactions, mainly due to the limited resolution of these previous structures<sup>12,13,21</sup>. In this study, we purified the predominant form of  $\text{SCI}_1\text{III}_2\text{IV}_1$  from porcine heart, and obtained a 5.4 Å resolution structure using single-particle cryo-electron microscopy (cryo-EM). Our structure reveals the precise placement of complexes in  $\text{SCI}_1\text{III}_2\text{IV}_1$ , and establishes the inter-complex interactions between the respiratory chain complexes.

## Protein purification and structure determination

The supercomplexes were purified from bovine, porcine, rat and mouse hearts essentially as previously described<sup>11–14</sup>. The supercomplex from porcine heart solubilized with digitonin was used for final sample preparation and structural determination. BNPA analyses detected several forms of supercomplexes, with a predominant form migrating at 1.7 MDa which is consistent with the estimated size of  $\text{SCI}_1\text{III}_2\text{IV}_1$  (Extended Data Fig. 1). This band of  $\text{SCI}_1\text{III}_2\text{IV}_1$  could be stained with nitro blue tetrazolium (NBT) dye that is specific to active CI, indicating that CI in this supercomplex had NADH dehydrogenase enzymatic activity (Extended Data Fig. 1b, e).

The initial three-dimensional (3D) reference of the 1.7 MDa respirasome was created by negative staining electron microscopy (EM). As shown in Extended Data Fig. 2, the initial model shows an F-shaped structure similar to those previously described<sup>12,13,21</sup>. High-resolution images were recorded on a Titan Krios TEM equipped with a Falcon II camera (Extended Data Fig. 3a–c). Classification of raw cryo-EM particles resulted in well-resolved 2D class averages, with some

<sup>1</sup>Ministry of Education Key Laboratory of Protein Science, Tsinghua-Peking Joint Center for Life Sciences, Beijing Advanced Innovation Center for Structural Biology, School of Life Sciences, Tsinghua University, Beijing 100084, China.

\*These authors contributed equally to this work.

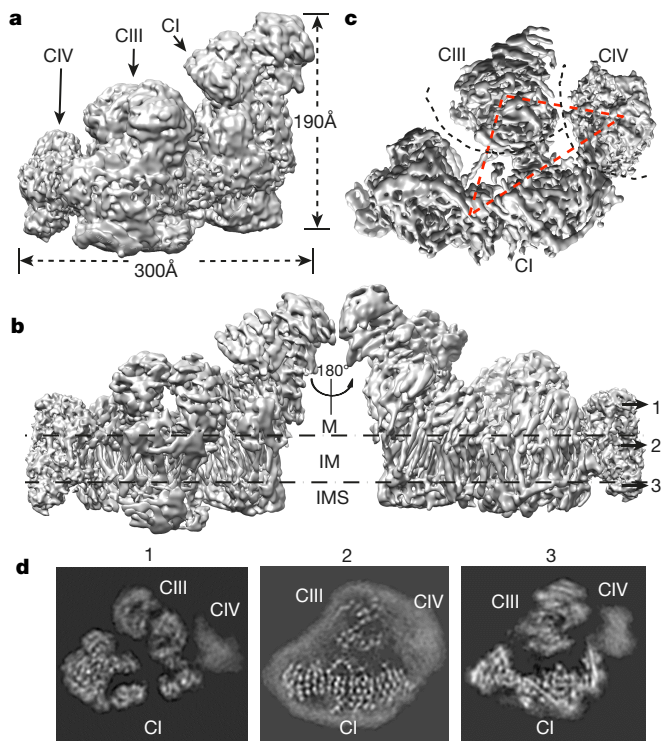


**Figure 1 | Cryo-EM structure of the respirasome.** **a**, The side views along the membrane of the unsharpened density map (at  $5\sigma$  contour level) of the respirasome with distinct regions labelled and indicated by black arrows. **b**, Same as **d**, but for the sharpened map filtered to a resolution of 5.4 Å ( $7\sigma$  contour level of CI and CIII;  $5\sigma$  contour level of CIV). The transmembrane region is indicated by two dashed lines. M, matrix; IM, inner membrane; IMS, intermembrane space. **c**, Bottom view of the unsharpened map viewed from the intermembrane space. The black dashed lines indicate the boundaries between the complexes. The red dashed lines linked the centres of the transmembrane regions of three complexes. **d**, Selected  $z$  slices of the final sharpened map corresponding to the layers indicated by the numbered arrows in **b**. The arrays of transmembrane segments could be easily seen in subpanel 2. The positions of different complexes are indicated.

secondary structural features clearly discernable (Extended Data Fig. 3d). After 3D classification of particles (Extended Data Fig. 4), a subset of particles was subjected to high-resolution refinement, resulting in a 3D density map with a final overall resolution of 5.4 Å (Gold-standard FSC 0.143 criterion), with higher resolutions in the centre and lower resolutions in the periphery (Fig. 1a–c and Extended Data Figs 4 and 5).

The F-shaped density map can be clearly divided into three parts, with an elongated part located underneath two spherical parts (Fig. 1). The diameter determined from the top view and the axial height of the structure are  $\sim 300$  Å and 190 Å, respectively. Subregion refinement with two different masks corresponding to CI and CIII, respectively, further improved the density map of CI and CIII to a resolution of  $\sim 3.9$ –4.0 Å (gold-standard FSC 0.143 criterion) (Extended Data Fig. 6a). From the density map, the transmembrane region can be readily identified, as it features many density rods (Fig. 1b–d). The local resolution map shows that the transmembrane helices are among the best-resolved regions, except those in CIV (Extended Data Fig. 5a). Subsequent docking of the 5.0 Å cryo-EM model of the bovine CI (PDB accession code 4UQ8)<sup>23</sup> and the high-resolution crystal structures of the CIII homodimer (PDB accession code 1BGY)<sup>24</sup> and the CIV monomer (PDB accession code 1OCC)<sup>25</sup> into the map resulted in high correlation coefficients. The resulting model was further optimized manually using Coot<sup>26</sup> (Fig. 2a and Extended Data Fig. 6b, c).

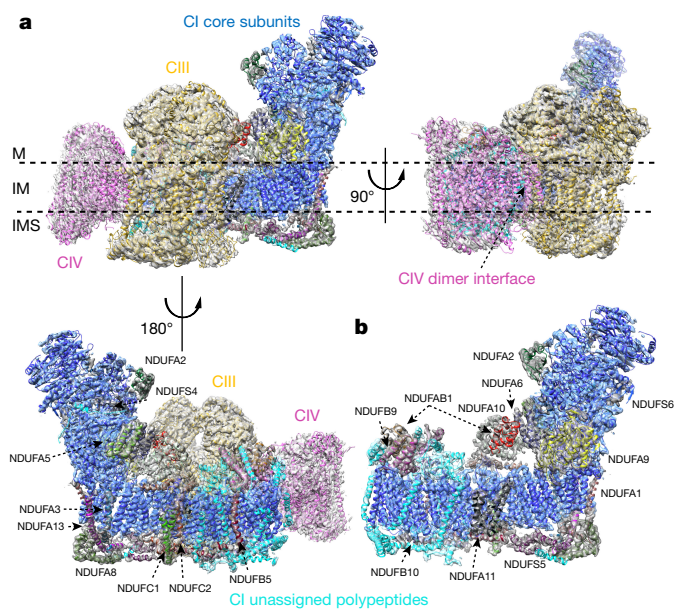


**Figure 2 | Assignment of the SCI<sub>1</sub>III<sub>2</sub>IV<sub>1</sub>.** **a**, Transparent surface representation of the segmented maps of different components, shown in three views along the membrane with different rotations. The structures of the core subunits and unassigned supernumerary components of CI are shown in cartoon representation and coloured in blue and cyan, respectively. The assigned subunits are coloured in different colours and indicated. CIII and CIV are coloured in golden and magenta, respectively. **b**, CI is shown the same as in **a** and with the assigned supernumerary components as indicated.

### Assignment of CI

The structure and function of CI have been subject to intensive investigations for decades<sup>23,27–32</sup>. The mammalian CI is the largest and most complex enzyme in the inner mitochondrial membrane. The overall structure of CI is about 190 Å in height and 250 Å in length, and contains 44 different subunits with two copies of NDUFAB1. It was reported that the 14 conserved core subunits form an L-shaped structure<sup>23,28,30,31</sup> that catalyses the energy-transducing reactions. The 7 matrix domain core subunits surrounded by 10 supernumerary subunits protrude out of the membrane to form the matrix arm. The 7 membrane arm core subunits are buried in the mitochondrial inner membrane, with 21 additional supernumerary subunits encircling them, and 14 of these supernumerary components have at least one transmembrane domain. The 3.97 Å density map of the CI alone allowed us to build the model with the side chain for the majority of residues from the core subunits, especially in the membrane arm region. The density for the side chains is well resolved in tightly packed subunits, but the density for the distal end of the peripheral regions is less ordered (Fig. 2 and Extended Data Fig. 6b, c). In the structure, we were able to accurately place 14 core subunits and 20 supernumerary subunits. Furthermore, we have built the model for additional 17 backbone models into the unoccupied density, which should belong to the other 11 unassigned supernumerary components and/or the unassigned regions of the assigned proteins (Figs 2 and 3a). In total, the structure of CI contains 77 transmembrane helices in the membrane domain. Compared with the previously reported bovine structure (PDB accession code 4UQ8), one transmembrane helix at the distal end of the membrane arm beside ND5 is not detected in our structure.

The CI can be separated into four functional modules. The distal half of the matrix arm forms the N module, comprising the core subunits NDUFV1, NDUFV2 and NDUFS1, and the supernumerary subunits NDUFS6 and NDUFA2. The N module contains a FMN molecule to oxidize NADH. The proximal half of the matrix arm forms another functional module that docks onto the membrane arm of CI (Fig. 3), made of the core subunits NDUFS2, NDUFS3, NDUFS7 and NDUFS8,

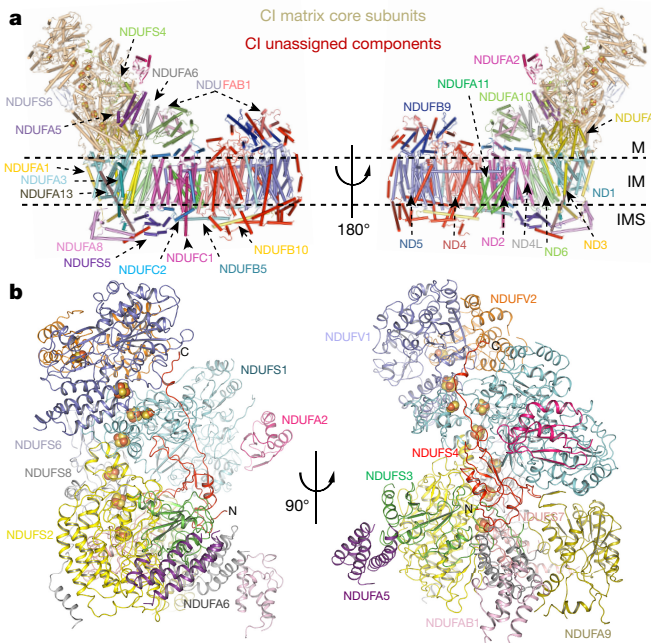


**Figure 3 | Overall structure of CI.** **a**, The overall structure of the CI. Cartoon representation of the CI structure in views along the membrane with different rotations. The structures of the core subunits of the matrix region, the unassigned components of CI, and the assigned subunits are coloured individually as indicated. The FeS clusters are shown in spheres. **b**, The matrix region of CI. Different subunits are coloured individually as indicated.

and the supernumerary subunits NDUFA5, NDUFA6, NDUFA9 and NDUFAB1. The NDUFS4 supernumerary subunit interacts with all the core subunits from both two matrix modules by bridging them together (Fig. 3b). The membrane arm comprises another two modules. The core subunits ND5 and ND4, together with several supernumerary components, form the two distal antiporter-like proton pump module ( $P_D$ ). The core subunits ND2, ND4L, ND6, ND3 and ND1, together with the other supernumerary subunits, constitute the proximal pump module ( $P_P$ ), which contains two additional proton pumps and is combined with the matrix arm (Fig. 3a).

### Assignment of CIII and CIV

Beside the membrane arm of CI, an area of density with an approximate twofold symmetry (160 Å in height and 140 Å in width) could be easily assigned to a CIII homodimer (PDB accession code 1BGY)<sup>24</sup> (Fig. 2a). This assignment is consistent with dimeric CIII being the central component of the mitochondrial respiratory chain, transferring electrons from ubiquinone to cytochrome *c* and generating a proton gradient across the inner mitochondrial membrane<sup>6,7</sup>. Previous studies demonstrated that the functional domains of Rieske iron-sulfur protein (ISP) subunits in CIII have different positions in distinct structural forms, termed '*c*', '*b*' and '*int*' (intermediate) states, corresponding to the different distances from the [2Fe-2S] cluster to haem *c*<sub>1</sub> or haem *b*<sub>L</sub><sup>24,33,34</sup>. The relative distances of [2Fe-2S]-haem *c*<sub>1</sub> and [2Fe-2S]-haem *b*<sub>L</sub> in the final refined density map are 30 Å and 27 Å, respectively (Extended Data Fig. 6d), indicating that the CIII dimer in our structure is in the intermediate state.

In the structure, each CIII monomer contains 11 different polypeptides with a total mass of about 240 kDa. The two-fold axis of the CIII homodimer is oriented perpendicular to the membrane plane of the CI membrane arm. The matrix domains of the CIII dimer protrude about 75 Å out of the membrane plane at the matrix side and face the hydrophilic arm of CI (Fig. 2a). At the intermembrane space, the outward surfaces of CIII are almost horizontal to the exterior surfaces

of supernumerary proteins in the membrane arm of CI at same side (Fig. 2a). However, there is no density at either of the expected cytochrome *c* binding sites on the exterior surfaces of CIII at the intermembrane space (Extended Data Fig. 7), suggesting that cytochrome *c* might be lost during sample purification.

A rectangular-shaped density positioned at the distal end of the membrane arm of CI and adjacent to the CIII dimer has a dimension of 90, 60 and 120 Å (Fig. 2a), consistent with that of a CIV monomer. Rigid body fitting of the 13 subunits of the crystal structure of CIV (PDB accession code 1OCC) indicates that the COX4I1 and COX5A subunits protrude towards the matrix side, with the expected cytochrome *c* binding site located at the intermembrane side. The dimerization interface of CIV at the concave side in the crystal structures faces outwards from the entire supercomplex, raising the possibility that CIV in the respirasome could form a homodimer in higher-order assemblies (Fig. 2a, right).

It has been reported<sup>23–25</sup> that SCI<sub>1</sub>III<sub>2</sub>IV<sub>1</sub> contains 69 different polypeptides and is made of 81 protein chains, with 45 from CI, 22 from dimeric CIII and 14 from CIV. Our density map suggests the existence of additional densities for unassigned supernumerary components and/or the unassigned regions of the assigned proteins of CI, although the moderate resolution of our map does not allow us to determine their identities. Nevertheless, we could build 17 backbone chains into the unoccupied density located at the transmembrane and peripheral regions in CI. This results in 131 transmembrane helices in our respirasome structure, with 77 from CI, 26 from CIII and 28 from CIV (Figs 2, 3 and 4a). The transmembrane regions of the three complexes forms a gigantic transmembrane disk with a flat surface on the intermembrane side (Figs 1a–c and 2a and Extended Data Fig. 7).

### Interaction between CI and CIII

Structural analyses indicate that the NDUFA11 subunit directly interacts with both CI and CIII (Fig. 4b). The NDUFA11 contains four transmembrane helices in the middle, with a short helix at the N terminus and a loop region at the C terminus (Extended Data Fig. 8a). The four transmembrane helices form a four-helix bundle roughly in parallel with the transmembrane helices of the middle of the membrane arm of CI. The N-terminal of NDUFA11 and the C-terminal ends of transmembrane helix 1 (TMH1) mainly interact with the C-terminal end of the HL helix and the last helix of ND5. The C-terminal end of transmembrane helix 4 (TMH4) interacts with the ND4. The C-terminal loop mainly contacts with ND2 at the intermembrane space (Fig. 4b). The other side of NDUFA11 faces the transmembrane region of CIII, close to the UQCRCB and UQCRCQ subunits of one monomer of the CIII dimer (Fig. 4b). These structural observations are consistent with previous studies showing that a mutation disrupting the first transmembrane helix of NDUFA11 destabilized the entire complex<sup>35</sup>, and that suppression of NDUFA11 expression disrupted the assembly of CI, resulting in the accumulation of 550 kDa and 815 kDa CI sub-complexes and failure to form supercomplexes<sup>27</sup>.

The LYR-motif-containing supernumerary component NDUFB9 and a SDAP acyl-carrier protein, NDUFAB1, are located on the distal end of the membrane arm, on top of ND5 at the matrix side of CI. NDUFAB1 binds into the groove between the N- and C-lobe of NDUFB9, and the N-lobe of NDUFB9 mainly contribute to the CI-CIII interaction (Extended Data Fig. 8b). A short loop (UQCRC1<sup>S251-L265</sup>) on the matrix side of the UQCRC1 subunit of the other CIII monomer inserts into the groove formed by the N-lobe of NDUFB9 and an unassigned supernumerary protein (Fig. 4c). The LYR motif in the N-lobe of NDUFB9 is important for NDUFAB1 binding<sup>36</sup>, and could be crucial for stabilizing the CI and CIII interaction as well. This hypothesis is consistent with the previous finding that mutations on NDUFB9 caused CI deficiency<sup>37</sup>, disturbance of the NAD<sup>+</sup>/NADH balance and promotion of tumour metastasis<sup>38</sup>. There are two unassigned transmembrane helices between CI and CIII (Fig. 4b), which probably belong to unassigned supernumerary components required

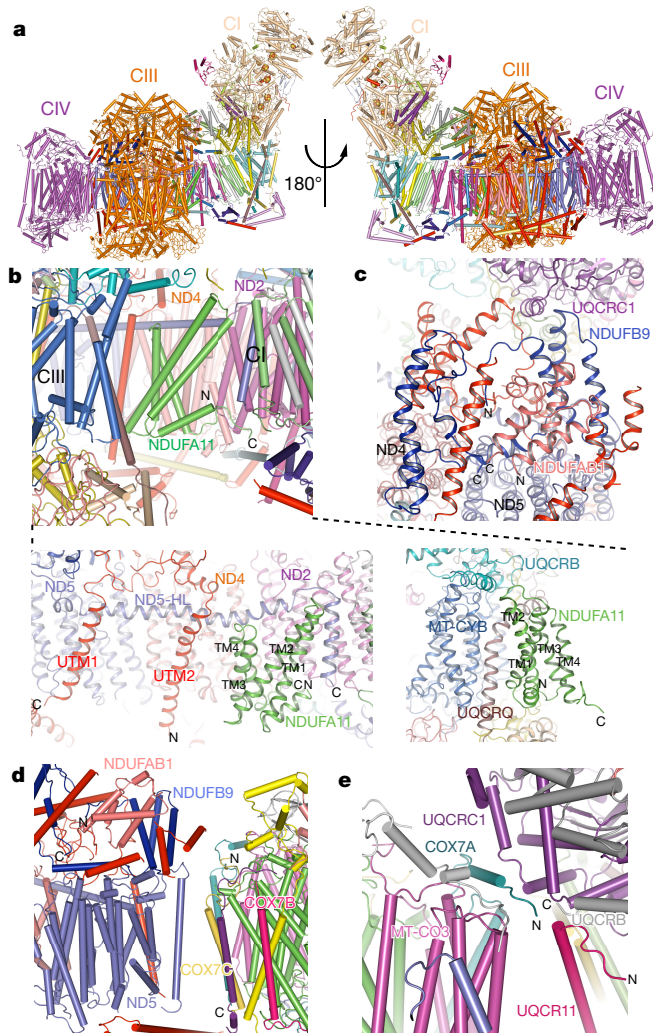


**Figure 4 | Interaction between the three complexes.** **a**, Overall model of the respirasome. The core, assigned and unassigned subunits of CI are indicated. CIII and CIV are coloured in gold and magenta, respectively. The FeS clusters in the matrix region of CI are shown in spheres. The view along the membrane is presented. **b**, NDUFA11 interacts with both CI and CIII. Different subunits are coloured individually as indicated. The two lower images respectively show the individual interactions between NDUFA11 with CI and CIII. UTM, unassigned transmembrane helix. **c**, The UQCRC1 of CIII interacts with the supernumerary components of CI at the distal end of the membrane arm. The unassigned supernumerary components are coloured in red and the other different supernumerary subunits are coloured individually as indicated. **d**, Interactions between CI and CIV. Different subunits are coloured individually as indicated in the same colours as in **b**. **e**, The interaction between CIII and CIV.

for the oligomerization of CI and CIII. Sequence alignments reveal that the binding motifs of NDUFA11, NDUFB9 and UQCRC1 are highly conserved across species (Extended Data Fig. 9), indicating that the arrangement of individual complexes within the respirasome is probably highly conserved.

### Interaction with CIV

Although the supernumerary components of CI contribute to the interaction between CI and CIII, they are not directly involved in the interaction between CI and CIV. Instead, the CI–CIV interaction is mainly mediated by packing of the transmembrane helix of COX7C subunit of CIV against the last transmembrane helix of ND5 at the distal end of the membrane arm of CI (Fig. 4d). Additionally, the flexible region before the transmembrane helix of COX7A makes contacts with both UQCRC1 and UQCRR11 at the matrix side (Fig. 4e), further

strengthening the interaction between CIII and CIV. Consistent with these structural observations, the cytochrome *c* oxidase subunit VIIa polypeptide 2 like (Cox7-a2L) is required for the CIII–CIV interaction<sup>39–41</sup>. The Cox7-a2L isoform, a naturally occurring mutation of this protein in the mouse strain C57BL/6, could directly affect the formation of SCIII<sub>2</sub>IV<sub>1</sub> (ref. 41) instead of directly affecting the formation of SCII<sub>1</sub>III<sub>2</sub>IV<sub>1</sub>, as previously described<sup>42</sup>. Compared to the supernumerary proteins which act as bridges for direct association between CI and CIII, CIV has slightly weaker interactions with both CI and CIII, which could be the main factor hampering high-resolution structural determination of this region (Extended Data Fig. 5a).

A previous study based on a low-resolution structure suggested that the cytochrome *b*, Rieske and UQCR11 of CIII could interact with COX3, COX6A and COX7A of CIV, respectively<sup>21</sup>. The interaction between COX7A and UQCR11 was confirmed in our structure, however, the distances of cytochrome *b* and Rieske in CIII to COX3 and COX6A in CIV are in the range of 10–30 Å, indicating that they probably do not have direct interactions. Moreover, there are clear gaps between the three complexes and no discernable interactions at the intermembrane space side (Fig. 1c). As a large amount of different lipid bilayer components, such as cardiolipin, phosphatidylcholine and phosphatidylethanolamine, should be present in the purified complexes<sup>11,43,44</sup>, we propose that these lipid bilayer components may occupy the space between the complexes to further stabilize the respirasome.

Interestingly, at the intermembrane side, the cytosolic surfaces of all three complexes are positioned in the same horizontal plane (Figs 1a–c and 2a and Extended Data Fig. 7). We propose that this orientation of the respirasome, especially the flat faces of CIII and CIV, could facilitate the translocation of reduced cytochrome *c*.

### The conformational change of CI

Structural comparison reveals that CI in the respirasome is more compact than the free CI (PDB accession code 4UQ8)<sup>23</sup> (Extended Data Fig. 10a). Although the ND3, ND4, ND4L and ND6 subunits at the middle region of the membrane arm remain largely unchanged, the matrix domain (Extended Data Fig. 10b) and the ND4 and ND5 subunits at the distal end of the membrane arm display a lateral movement towards the middle region (Extended Data Fig. 10c). These coordinated conformational changes are consistent with an earlier proposal that a conformational change of CI in the respirasome is needed to accommodate the binding of CIII and CIV (ref. 45).

### Conclusions

The structure and function of the mitochondrial respiratory chain have been extensively investigated for decades. Previous studies suggested several different assembly models for the respiratory chain complexes, such as the random collision model<sup>46</sup>, solid state model<sup>47</sup> and plasticity model<sup>42</sup>. More recent investigations by genetic, BNPA electrophoresis and single-particle EM studies<sup>4,10,12,13,19,21</sup>, supported the plasticity model and demonstrated the existence of different supramolecular assemblies. Previous electron tomography and freeze-fracture EM studies indicated that the respiratory complexes form higher-order assemblies of respiratory rows or strings<sup>48,49</sup>. Unlike the linearly arrayed complex V dimer on the cristae<sup>50</sup>, the nature and composition of the respiratory string are not well defined, probably due to difficulties in maintaining the transient strings after detergent solubilization. We and others have detected higher-molecular-weight bands above the SCII<sub>1</sub>III<sub>2</sub>IV<sub>1</sub> (Extended Data Fig. 1b)<sup>12,16,21,22</sup>, suggesting that the respiratory supercomplexes could exist in higher oligomeric states. Together, our near atomic cryo-EM map of the respiratory chain SCII<sub>1</sub>III<sub>2</sub>IV<sub>1</sub> now establishes the spatial arrangement of CI, dimeric CIII and CIV, offers a blueprint for studying the coordination between individual complexes during electron transfer, and provides new insights into the respiratory string organization.

**Online Content** Methods, along with any additional Extended Data display items and Source Data, are available in the online version of the paper; references unique to these sections appear only in the online paper.

Received 2 March; accepted 11 August 2016.

Published online 21 September; corrected online 28 September 2016  
(see full-text HTML version for details).

1. Visconti, C., Bottani, E. & Zeviani, M. Emerging concepts in the therapy of mitochondrial disease. *Biochim. Biophys. Acta* **1847**, 544–557 (2015).
2. Wallace, D. C. Mitochondrial DNA variation in human radiation and disease. *Cell* **163**, 33–38 (2015).
3. Wallace, D. C. & Chalkia, D. Mitochondrial DNA genetics and the heteroplasmy conundrum in evolution and disease. *Cold Spring Harb. Perspect. Biol.* **5**, a021220 (2013).
4. Schägger, H. & Pfeiffer, K. The ratio of oxidative phosphorylation complexes I–V in bovine heart mitochondria and the composition of respiratory chain supercomplexes. *J. Biol. Chem.* **276**, 37861–37867 (2001).
5. Lenaz, G. & Genova, M. L. Structure and organization of mitochondrial respiratory complexes: a new understanding of an old subject. *Antioxid. Redox Signal.* **12**, 961–1008 (2010).
6. Sone, N., Sekimachi, M. & Kuroh, E. Identification and properties of a quinol oxidase super-complex composed of a bc<sub>1</sub> complex and cytochrome oxidase in the thermophilic bacterium PS3. *J. Biol. Chem.* **262**, 15386–15391 (1987).
7. Berry, E. A. & Trumper, B. L. Isolation of ubiquinol oxidase from *Paracoccus denitrificans* and resolution into cytochrome bc<sub>1</sub> and cytochrome c-aa<sub>3</sub> complexes. *J. Biol. Chem.* **260**, 2458–2467 (1985).
8. Schägger, H. Respiratory chain supercomplexes. *IUBMB Life* **52**, 119–128 (2001).
9. Schägger, H. & Pfeiffer, K. Supercomplexes in the respiratory chains of yeast and mammalian mitochondria. *EMBO J.* **19**, 1777–1783 (2000).
10. Dudkina, N. V., Eubel, H., Keegstra, W., Boekema, E. J. & Braun, H. P. Structure of a mitochondrial supercomplex formed by respiratory-chain complexes I and III. *Proc. Natl Acad. Sci. USA* **102**, 3225–3229 (2005).
11. Shinzawa-Itoh, K. et al. Purification of active respiratory supercomplex from bovine heart mitochondria enables functional studies. *J. Biol. Chem.* **291**, 4178–4184 (2016).
12. Althoff, T., Mills, D. J., Popot, J. L. & Kühlbrandt, W. Arrangement of electron transport chain components in bovine mitochondrial supercomplex I<sub>1</sub>III<sub>2</sub>IV<sub>1</sub>. *EMBO J.* **30**, 4652–4664 (2011).
13. Schäfer, E., Dencher, N. A., Vonck, J. & Pearcey, D. N. Three-dimensional structure of the respiratory chain supercomplex I<sub>1</sub>III<sub>2</sub>IV<sub>1</sub> from bovine heart mitochondria. *Biochemistry* **46**, 12579–12585 (2007).
14. Acín-Pérez, R., Fernández-Silva, P., Peleato, M. L., Pérez-Martos, A. & Enriquez, J. A. Respiratory active mitochondrial supercomplexes. *Mol. Cell* **32**, 529–539 (2008).
15. Acín-Pérez, R. et al. Respiratory complex III is required to maintain complex I in mammalian mitochondria. *Mol. Cell* **13**, 805–815 (2004).
16. Stroh, A. et al. Assembly of respiratory complexes I, III, and IV into NADH oxidase supercomplex stabilizes complex I in *Paracoccus denitrificans*. *J. Biol. Chem.* **279**, 5000–5007 (2004).
17. Diaz, F., Fukui, H., Garcia, S. & Moraes, C. T. Cytochrome c oxidase is required for the assembly/stability of respiratory complex I in mouse fibroblasts. *Mol. Cell. Biol.* **26**, 4872–4881 (2006).
18. Wittig, I., Carrozzo, R., Santorelli, F. M. & Schägger, H. Supercomplexes and subcomplexes of mitochondrial oxidative phosphorylation. *Biochim. Biophys. Acta* **1757**, 1066–1072 (2006).
19. Bultema, J. B., Braun, H. P., Boekema, E. J. & Kouril, R. Megacomplex organization of the oxidative phosphorylation system by structural analysis of respiratory supercomplexes from potato. *Biochim. Biophys. Acta* **1787**, 60–67 (2009).
20. Wittig, I. & Schägger, H. Supramolecular organization of ATP synthase and respiratory chain in mitochondrial membranes. *Biochim. Biophys. Acta* **1787**, 672–680 (2009).
21. Dudkina, N. V., Kudryashev, M., Stahlberg, H. & Boekema, E. J. Interaction of complexes I, III, and IV within the bovine respirasome by single particle cryoelectron tomography. *Proc. Natl Acad. Sci. USA* **108**, 15196–15200 (2011).
22. Schäfer, E. et al. Architecture of active mammalian respiratory chain supercomplexes. *J. Biol. Chem.* **281**, 15370–15375 (2006). 10
23. Vinothkumar, K. R., Zhu, J. & Hirst, J. Architecture of mammalian respiratory complex I. *Nature* **515**, 80–84 (2014).
24. Iwata, S. et al. Complete structure of the 11-subunit bovine mitochondrial cytochrome bc<sub>1</sub> complex. *Science* **281**, 64–71 (1998).
25. Tsukihara, T. et al. The whole structure of the 13-subunit oxidized cytochrome c oxidase at 2.8 Å. *Science* **272**, 1136–1144 (1996).
26. Emsley, P. & Cowtan, K. Coot: model-building tools for molecular graphics. *Acta Crystallogr. D* **60**, 2126–2132 (2004).
27. Andrews, B., Carroll, J., Ding, S., Fearnley, I. M. & Walker, J. E. Assembly factors for the membrane arm of human complex I. *Proc. Natl Acad. Sci. USA* **110**, 18934–18939 (2013).
28. Baradaran, R., Berrisford, J. M., Minhas, G. S. & Sazanov, L. A. Crystal structure of the entire respiratory complex I. *Nature* **494**, 443–448 (2013).
29. Berrisford, J. M. & Sazanov, L. A. Structural basis for the mechanism of respiratory complex I. *J. Biol. Chem.* **284**, 29773–29783 (2009).
30. Efremov, R. G., Baradaran, R. & Sazanov, L. A. The architecture of respiratory complex I. *Nature* **465**, 441–445 (2010).
31. Efremov, R. G. & Sazanov, L. A. Structure of the membrane domain of respiratory complex I. *Nature* **476**, 414–420 (2011).
32. Sazanov, L. A. & Hinchliffe, P. Structure of the hydrophilic domain of respiratory complex I from *Thermus thermophilus*. *Science* **311**, 1430–1436 (2006).
33. Zhang, Z. et al. Electron transfer by domain movement in cytochrome bc<sub>1</sub>. *Nature* **392**, 677–684 (1998).
34. Iwata, M., Björkman, J. & Iwata, S. Conformational change of the Rieske [2Fe-2S] protein in cytochrome bc<sub>1</sub> complex. *J. Bioenerg. Biomembr.* **31**, 169–175 (1999).
35. Berger, I. et al. Mitochondrial complex I deficiency caused by a deleterious NDUF11 mutation. *Ann. Neurol.* **63**, 405–408 (2008).
36. Angerer, H. et al. The LYR protein subunit NB4M/NDUF6 of mitochondrial complex I anchors an acyl carrier protein and is essential for catalytic activity. *Proc. Natl Acad. Sci. USA* **111**, 5207–5212 (2014).
37. Haack, T. B. et al. Mutation screening of 75 candidate genes in 152 complex I deficiency cases identifies pathogenic variants in 16 genes including NDUF9. *J. Med. Genet.* **49**, 83–89 (2012).
38. Tan, A. S., Baty, J. W. & Berridge, M. V. The role of mitochondrial electron transport in tumorigenesis and metastasis. *Biochim. Biophys. Acta* **1840**, 1454–1463 (2014).
39. Ikeda, K., Shiba, S., Horie-Inoue, K., Shimokata, K. & Inoue, S. A stabilizing factor for mitochondrial respiratory supercomplex assembly regulates energy metabolism in muscle. *Nature Commun.* **4**, 2147 (2013).
40. Williams, E. G. et al. Systems proteomics of liver mitochondria function. *Science* **352**, aad0189 (2016).
41. Mourier, A., Matic, S., Ruzzenente, B., Larsson, N. G. & Milenkovic, D. The respiratory chain supercomplex organization is independent of COX7a2L isoforms. *Cell Metab.* **20**, 1069–1075 (2014).
42. Lapuente-Brun, E. et al. Supercomplex assembly determines electron flux in the mitochondrial electron transport chain. *Science* **340**, 1567–1570 (2013).
43. Sharpley, M. S., Shannon, R. J., Draghi, F. & Hirst, J. Interactions between phospholipids and NADH:ubiquinone oxidoreductase (complex I) from bovine mitochondria. *Biochemistry* **45**, 241–248 (2006).
44. Pfeiffer, K. et al. Cardiolipin stabilizes respiratory chain supercomplexes. *J. Biol. Chem.* **278**, 52873–52880 (2003).
45. Radermacher, M. et al. The three-dimensional structure of complex I from *Yarrowia lipolytica*: a highly dynamic enzyme. *J. Struct. Biol.* **154**, 269–279 (2006).
46. Hackenbrock, C. R., Chazotte, B. & Gupte, S. S. The random collision model and a critical assessment of diffusion and collision in mitochondrial electron transport. *J. Bioenerg. Biomembr.* **18**, 331–368 (1986).
47. Chance, B. & Williams, G. R. Respiratory enzymes in oxidative phosphorylation. III. The steady state. *J. Biol. Chem.* **217**, 409–427 (1955).
48. Nicastro, D., Frangakis, A. S., Tyype, D. & Baumeister, W. Cryo-electron tomography of *Neurospora* mitochondria. *J. Struct. Biol.* **129**, 48–56 (2000).
49. Allen, R. D., Schroeder, C. C. & Fok, A. K. An investigation of mitochondrial inner membranes by rapid-freeze deep-etch techniques. *J. Cell Biol.* **108**, 2233–2240 (1989).
50. Davies, K. M. et al. Macromolecular organization of ATP synthase and complex I in whole mitochondria. *Proc. Natl Acad. Sci. USA* **108**, 14121–14126 (2011).

**Acknowledgements** We would like to thank the staff members X. Li, F. Yang and Y. Li of Tsinghua University Branch of China National Center for Protein Sciences (Beijing, China) for providing the facility support. This work was supported by funds from the Ministry of Science and Technology (2016YFA0501101 and 2012CB911101 to M.J., and 2013CB910404 and 2016YFA0500700 to N.G.), and the National Outstanding Young Scholar Science Foundation and National Natural Science Foundation of China (31030020 and 31170679 to M.Y., 31422016 to N.G.).

**Author Contributions** M.Y. conceived, designed and supervised the project, analysed data and wrote the manuscript. J.G. and R.G. did the protein purification and detergent screening. M.W. performed electron microscopy sample preparation, data collection and structural determination with help of K.Y., N.G. and J.L. All authors discussed the data and read the manuscript.

**Author Information** The 3D cryo-EM density map has been deposited in the Electron Microscopy Data Bank (EMDB), with accession code EMD-9534. The coordinates of atomic models have been deposited in the Protein Data Bank (PDB) under the accession code 5GPN for the respirasome. Reprints and permissions information is available at [www.nature.com/reprints](http://www.nature.com/reprints). The authors declare no competing financial interests. Readers are welcome to comment on the online version of the paper. Correspondence and requests for materials should be addressed to N.G. ([ninggao@tsinghua.edu.cn](mailto:ninggao@tsinghua.edu.cn)) and M.Y. ([maojunyang@tsinghua.edu.cn](mailto:maojunyang@tsinghua.edu.cn)).

**Reviewer Information** *Nature* thanks A. Engel, D. Winge, and the other anonymous reviewer(s) for their contribution to the peer review of this work.

## METHODS

**Data reporting.** No statistical methods were used to predetermine sample size. The experiments were not randomized. The investigators were not blinded to allocation during experiments and outcome assessment.

**Isolation of mitochondria from porcine heart.** All the following procedures were carried out on ice or at 4°C. Fresh porcine heart was obtained from the slaughterhouse and transported to the laboratory as soon as possible. 100 g of heart muscles were isolated and cut into small cubes. The heart muscles were washed twice with Milli-Q water and suspended in 100 ml of buffer A (100 mM Tris pH 7.4, 225 mM sorbitol, 60 mM KCl, 1 mM EGTA and 0.1% BSA). These tissues were homogenized in a large-capacity blender for 300 s. The homogenate was centrifuged at 3,000g for 20 min to remove cell debris. The supernatant was collected and applied to ultracentrifugation at 20,000g for 30 min to get the crude mitochondrial pellet. Crude mitochondria were suspended in 100 ml buffer B (50 mM Tris pH 7.4, 250 mM sucrose, 60 mM KCl, 40% Percoll and 0.1 mM EGTA) and centrifuged at 60,000g for 50 min. The mitochondrial band was aspirated carefully and diluted with 20 ml buffer C (50 mM Tris pH 7.4, 100 mM sorbitol, 60 mM KCl, 0.05 mM EGTA). The pure mitochondria were obtained, after centrifugation for 30 min at 20,000g. **Respiratory supercomplex purification.** The pure mitochondria were suspended in buffer C. After addition of 1% (w/v) digitonin, the sample was incubated overnight with slow stirring at 4°C. Ultracentrifugation was applied at 150,000g for 30 min. The collected supernatant was concentrated to 1 ml by 100 Kd cutoff centrifugal filter (Millipore). Then, the 1 ml sample was centrifuged on 0.3–1.8 M sucrose gradient in buffer D (25 mM Tris, pH 7.4, 60 mM KCl, 0.1% digitonin) at 150,000g for 20 h at 4°C using a SW41 rotor (Beckman). Gradients were fractionated and investigated by 3–10% BN-PAGE gel. The purified respiratory supercomplexes were concentrated and subjected to gel filtration chromatography (Superose 6 10/300 GL, GE Healthcare) in a buffer containing 10 mM Tris pH 7.4, 60 mM KCl and 0.1% digitonin (Extended Data Fig. 1c). The peak fractions were collected for electron microscopy analysis.

**Blue native PAGE.** Following the blue native PAGE protocol<sup>51</sup>, the purified respiratory supercomplexes were analysed using 3–10% a blue native PAGE mini gel (1.5 × 8.3 × 7.3 mm) for native electrophoresis at 150 V for 4 h (Extended Data Fig. 1a, d). **NBT staining.** Nitro blue tetrazolium (NBT) has two tetrazole moieties and is a soluble yellow chemical compound. When NBT is reduced, it forms blue or purple precipitate formazan. NBT staining can be used for specific in-gel activity assays of NADH dehydrogenase<sup>52</sup>. For NBT staining, BN-PAGE gels were incubated in buffer containing 100 mM Tris-glycine pH 7.4, 1 mg ml<sup>-1</sup> NBT and 100 μM β-NADH for 5 to 10 min (Extended Data Fig. 1b, e).

**Negative staining electron-microscopy.** 4 μl aliquots of respiratory supercomplexes (0.15 mg ml<sup>-1</sup>) were applied to glow discharged carbon-coated copper grids (300 mesh, Zhongjingkeyi, Beijing). After incubation for 1 min at room temperature, excessive liquid was absorbed by filter paper. Grids containing the specimen were stained by droplets of 2% uranyl acetate for 1 min, and air-dried. Micrographs were collected on a Tecnai Spirit microscope (FEI company) operated at a voltage of 120 kV, using a 4k × 4k charge-coupled device camera (CCD) (UltraScan 4000, Gatan). Images of respiratory supercomplexes purified with digitonin were recorded at a nominal magnification of ×68,000 and with a pixel size of 1.59 Å (Extended Data Fig. 2).

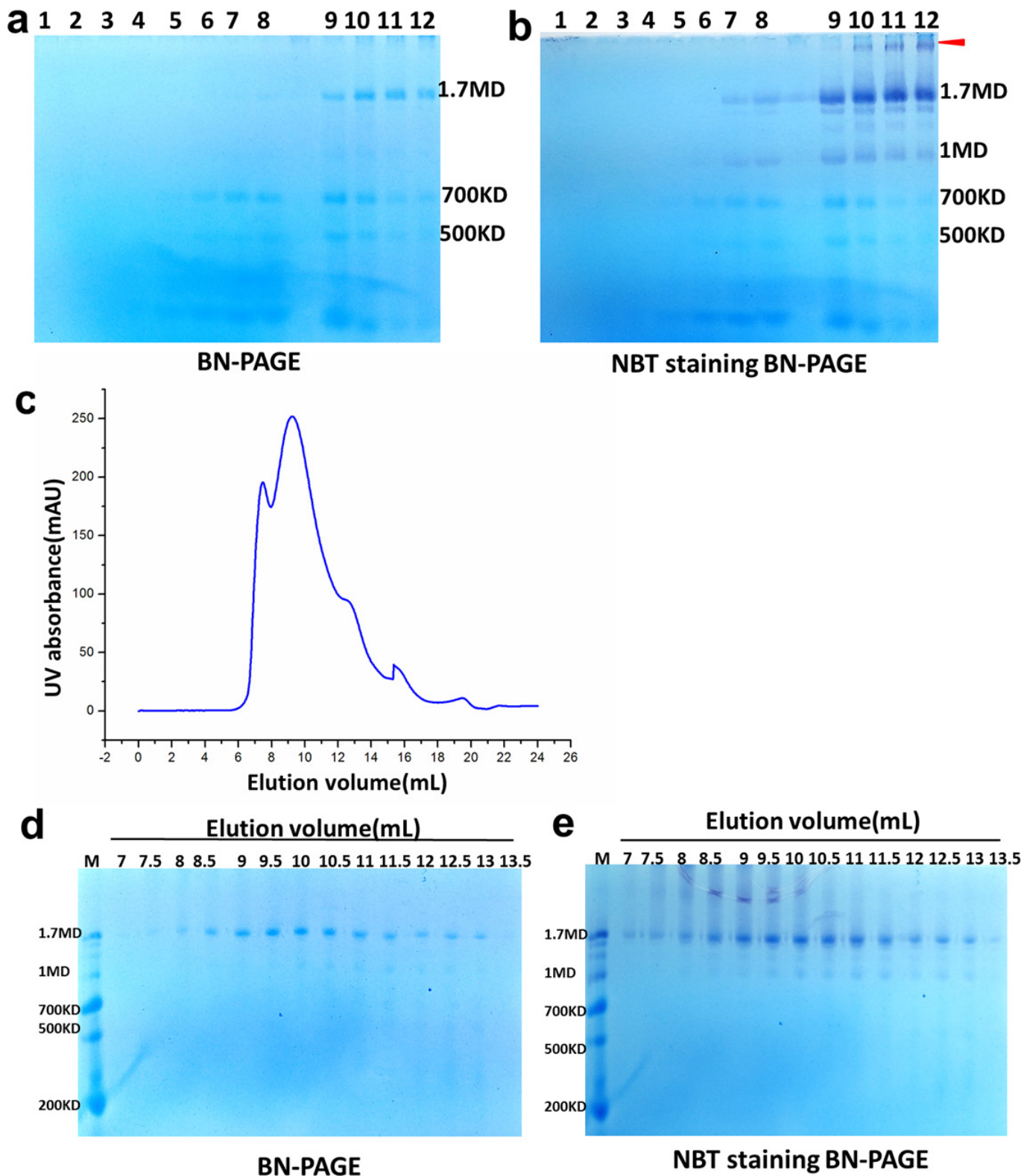
**Cryo-electron microscopy.** 4 μl aliquots of digitonin-solubilized respirasomes at a concentration of 0.2 mg ml<sup>-1</sup> were applied to glow-discharged 400-mesh Quantifoil R1.2/1.3 grids (Quantifoil, Micro Tools, Germany) coated with a home-made continuous thin carbon. Grids were blotted for 1.5 s and plunged into liquid ethane using an FEI Mark IV Vitrobot operated at 4°C and 100% humidity. High-resolution images were collected on an FEI Titan Krios microscope operated at a voltage of 300 kV with a Falcon II direct electron detector (FEI). Automated single-particle data acquisition was performed with EPU package (FEI), with a calibrated magnification of ×132,959 which yields a final pixel size of 1.05 Å at the object scale and with defocus ranging from −1.8 μm to −2.5 μm. A dose rate on the detector was about 42 electrons per pixel per second with a total exposure time of 1.2 s. Each micrograph stack contains 19 frames.

**Image processing.** The data sets of negative staining EM were processed with EMAN2.1 (ref. 53) and RELION1.4 (ref. 54). Reference-free 2D classification was performed with RELION. For negative staining EM data processing, particle picking was done with EMAN, particle classification, reconstruction and structural refinement were done with RELION. The final number of particles used in 3D classification is 9,936. A density ball was used as the initial reference for 3D classification. Of the three resulting classes, one containing 4,597 particles was used for refinement to generate a 3D model.

For Falcon II data sets processing, motion correction at micrograph level was done by the MotionCorr program (written by X. Li) to produce average micrographs over all frames<sup>55</sup>. Micrographs screening, particle picking and normalization were done with EMAN and RELION. The program CTFFIND3 (ref. 56) was used to estimate the contrast transfer function parameters. The 2D, 3D classification and refinement were

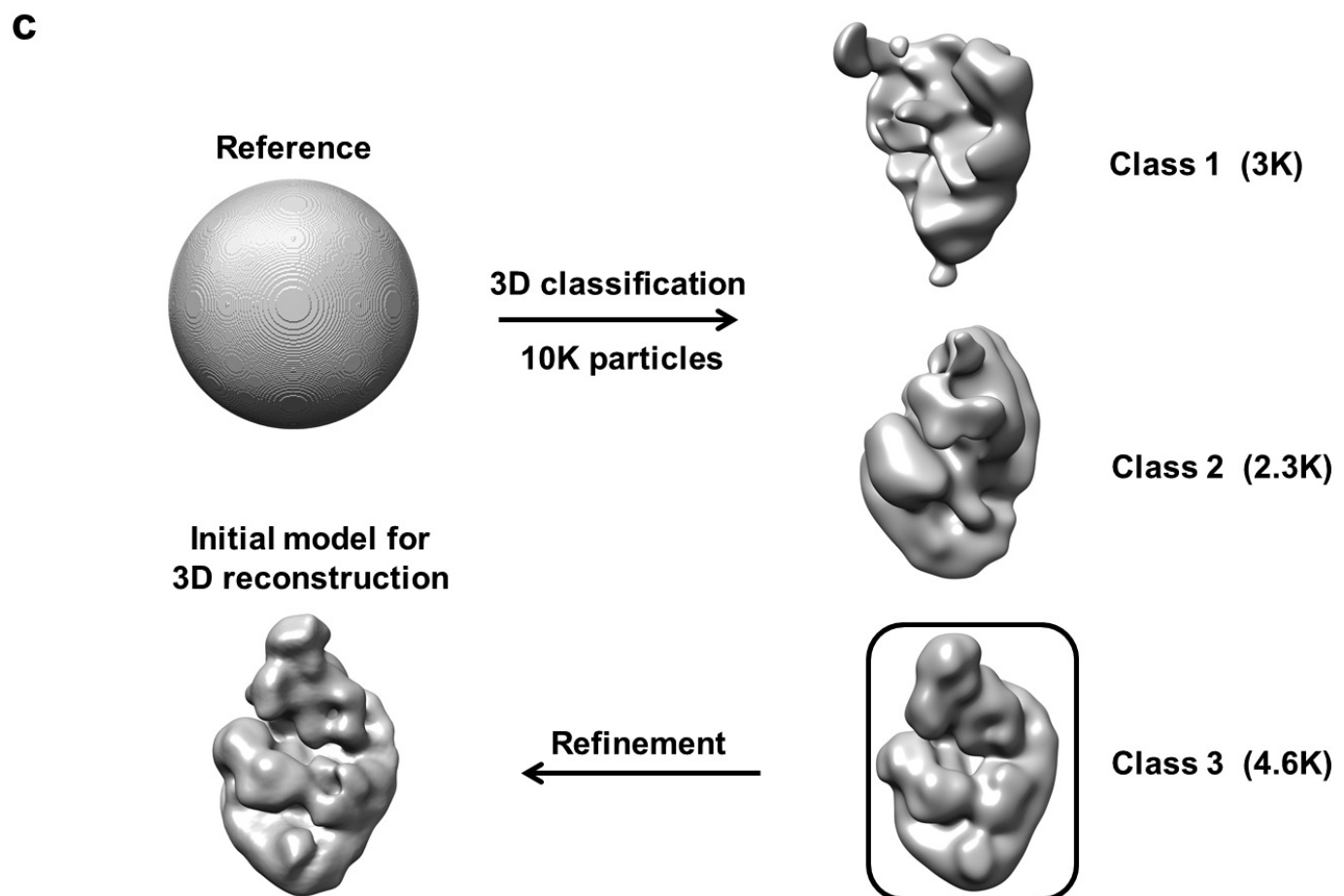
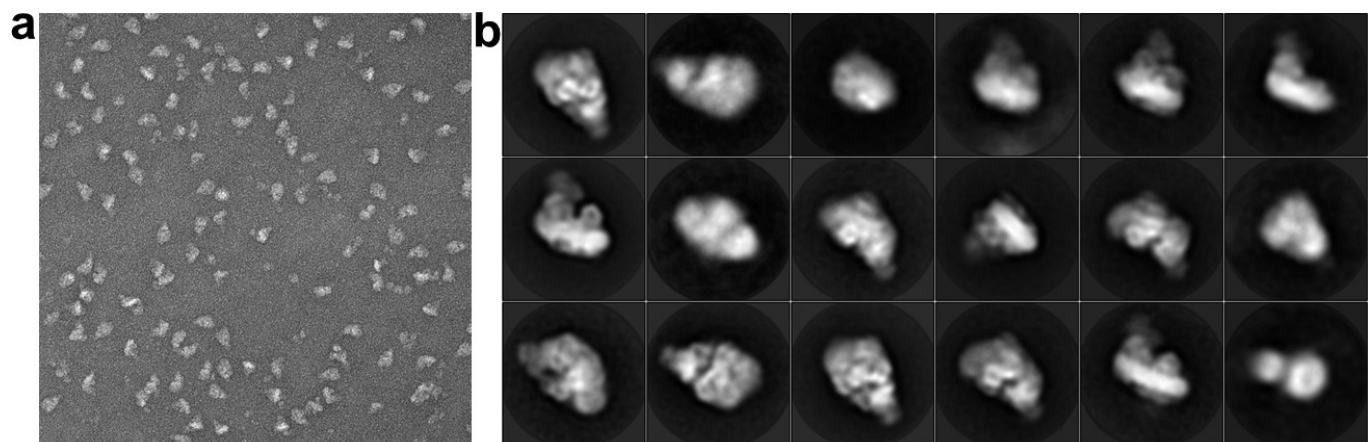
performed with RELION. 139,996 particles from 1,371 micrographs were subject to a cascade of 2D and 3D classification. Different combinations of particles from these classes were tested in refinement. A set of relatively homogeneous particles (50,370) were subjected to the final refinement, with negative staining model low-pass filtered to 60 Å as the initial reference. The refinement resulted in a density map at an overall resolution of 7.2 Å, with regions defined by the soft mask of the whole complex being 6.5 Å. Particles were rewindowed from the second to tenth frames of original micrograph stacks (motion corrections at the micrograph level were reperformed). Rewindowed particles were subjected to a second round of refinement using RELION, which improved the resolution of the region defined by the soft mask of the whole complex to 6.1 Å. A third round of refinement was done by applying an enlarged soft mask of the respirasome, and improved the resolution to 5.4 Å (Extended Data Fig. 5a, b). Further improvements of the density map were achieved by a set of soft-mask based subregion refinement procedures<sup>57</sup>, as previously described for ribosomal complex structural determination<sup>58–61</sup>. Specifically, enlarged soft masks for CI and CIII were created using the density map of the previous round, and applied during the subsequent masked-based refinement. Applying soft masks during 3D refinement would allow a better alignment of particles only according to structural features within the boundary defined by the mask. As a result, subregion refinement improved the density maps of CI and CIII to a resolution of 3.97 Å (Extended Data Figs 6a–c and 8). However, due to the weaker binding of CIV and its sub-stoichiometric occupancy in the supercomplexes, no significant improvement of the density map for CIV was obtained. All reported resolutions are based on the gold-standard FSC = 0.143 criteria<sup>62</sup>, and the final FSC curves were corrected for the effect of soft masks using high-resolution noise substitution<sup>63</sup>. Final density maps were sharpened by B-factor of −200 Å<sup>2</sup> using RELION. The local resolution map was calculated using ResMap<sup>64</sup>. **Model building and structural analyses.** Atomic models of the 14 conserved core subunits of *Sus scrofa* CI were predicted and modelled using the webserver (<http://www.sbg.bio.ic.ac.uk/phyre2>) of Phyre2 (ref. 65). Using the bovine CI structure (PDB accession code 4UQ8)<sup>23</sup> as the initial model, we assigned homology models of the 14 core subunits and 20 assigned subunits and 17 unassigned supernumerary polypeptides into our density maps. The models were further optimized by Coot (Extended Data Figs 6b, c and 8)<sup>26</sup>. Because the sequence similarity of CIII and CIV between *S. scrofa* and *Bos taurus* is very high (with sequence identity about 85–97%), we directly docked the crystal structures of the CII dimer (PDB accession code 1BGY)<sup>24</sup> and the CIV monomer (PDB accession code 1OCC)<sup>25</sup> into the map. Sequence alignment was carried out using DNAMAN. All the figures were created by UCSF Chimera<sup>66</sup>.

51. Wittig, I., Braun, H. P. & Schägger, H. Blue native PAGE. *Nature Protocols* **1**, 418–428 (2006).
52. Kuonen, D. R., Roberts, P. J. & Cottingham, I. R. Purification and analysis of mitochondrial membrane proteins on nondenaturing gradient polyacrylamide gels. *Anal. Biochem.* **153**, 221–226 (1986).
53. Tang, G. *et al.* EMAN2: an extensible image processing suite for electron microscopy. *J. Struct. Biol.* **157**, 38–46 (2007).
54. Scheres, S. H. RELION: implementation of a Bayesian approach to cryo-EM structure determination. *J. Struct. Biol.* **180**, 519–530 (2012).
55. Li, X. *et al.* Electron counting and beam-induced motion correction enable near-atomic-resolution single-particle cryo-EM. *Nature Methods* **10**, 584–590 (2013).
56. Mindell, J. A. & Grigorieff, N. Accurate determination of local defocus and specimen tilt in electron microscopy. *J. Struct. Biol.* **142**, 334–347 (2003).
57. Ge, J. *et al.* Architecture of the mammalian mechanosensitive Piezo1 channel. *Nature* **527**, 64–69 (2015).
58. Voorhees, R. M., Fernández, I. S., Scheres, S. H. & Hegde, R. S. Structure of the mammalian ribosome-Sec61 complex to 3.4 Å resolution. *Cell* **157**, 1632–1643 (2014).
59. Greber, B. J. *et al.* The complete structure of the large subunit of the mammalian mitochondrial ribosome. *Nature* **515**, 283–286 (2014).
60. Brown, A. *et al.* Structure of the large ribosomal subunit from human mitochondria. *Science* **346**, 718–722 (2014).
61. Fernández, I. S., Bai, X. C., Murshudov, G., Scheres, S. H. & Ramakrishnan, V. Initiation of translation by cricket paralysis virus IRES requires its translocation in the ribosome. *Cell* **157**, 823–831 (2014).
62. Scheres, S. H. & Chen, S. Prevention of overfitting in cryo-EM structure determination. *Nature Methods* **9**, 853–854 (2012).
63. Chen, S. *et al.* High-resolution noise substitution to measure overfitting and validate resolution in 3D structure determination by single particle electron cryomicroscopy. *Ultramicroscopy* **135**, 24–35 (2013).
64. Kucukelbir, A., Sigworth, F. J. & Tagare, H. D. Quantifying the local resolution of cryo-EM density maps. *Nature Methods* **11**, 63–65 (2014).
65. Kelley, L. A., Mezulis, S., Yates, C. M., Wass, M. N. & Sternberg, M. J. The Phyre2 web portal for protein modeling, prediction and analysis. *Nature Protocols* **10**, 845–858 (2015).
66. Pettersen, E. F. *et al.* UCSF Chimera—a visualization system for exploratory research and analysis. *J. Comput. Chem.* **25**, 1605–1612 (2004). 10.1002/jcc.20084
67. Solmaz, S. R. & Hunte, C. Structure of complex III with bound cytochrome c in reduced state and definition of a minimal core interface for electron transfer. *J. Biol. Chem.* **283**, 17542–17549 (2008).



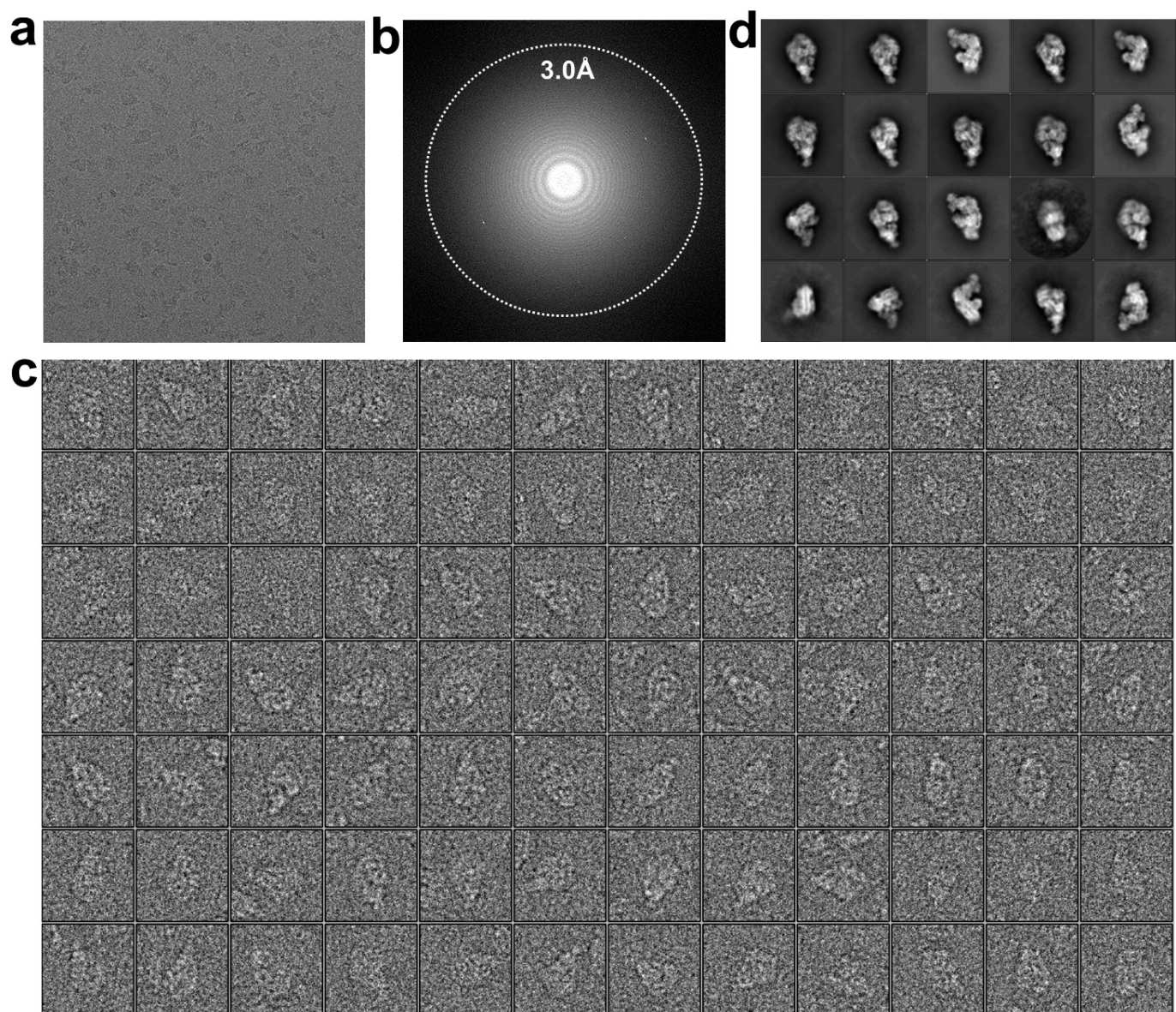
**Extended Data Figure 1 | Biochemical characterization of the respiratory supercomplexes.** **a**, Fractions of sucrose gradient ultracentrifugation were analysed by BNPA. **b**, In-gel staining of the native gel by NBT. Higher-molecular-weight bands were indicated by a red arrow. **c**, A representative trace of size-exclusion chromatography of

the respiratory supercomplexes. **d**, Protein samples of the size-exclusion chromatography fractions were subjected to BNPA. Fractions of 9–9.5 ml (elution volume) were used for negative staining EM and cryo-EM. **e**, NBT staining of the size-exclusion chromatography BNPA.

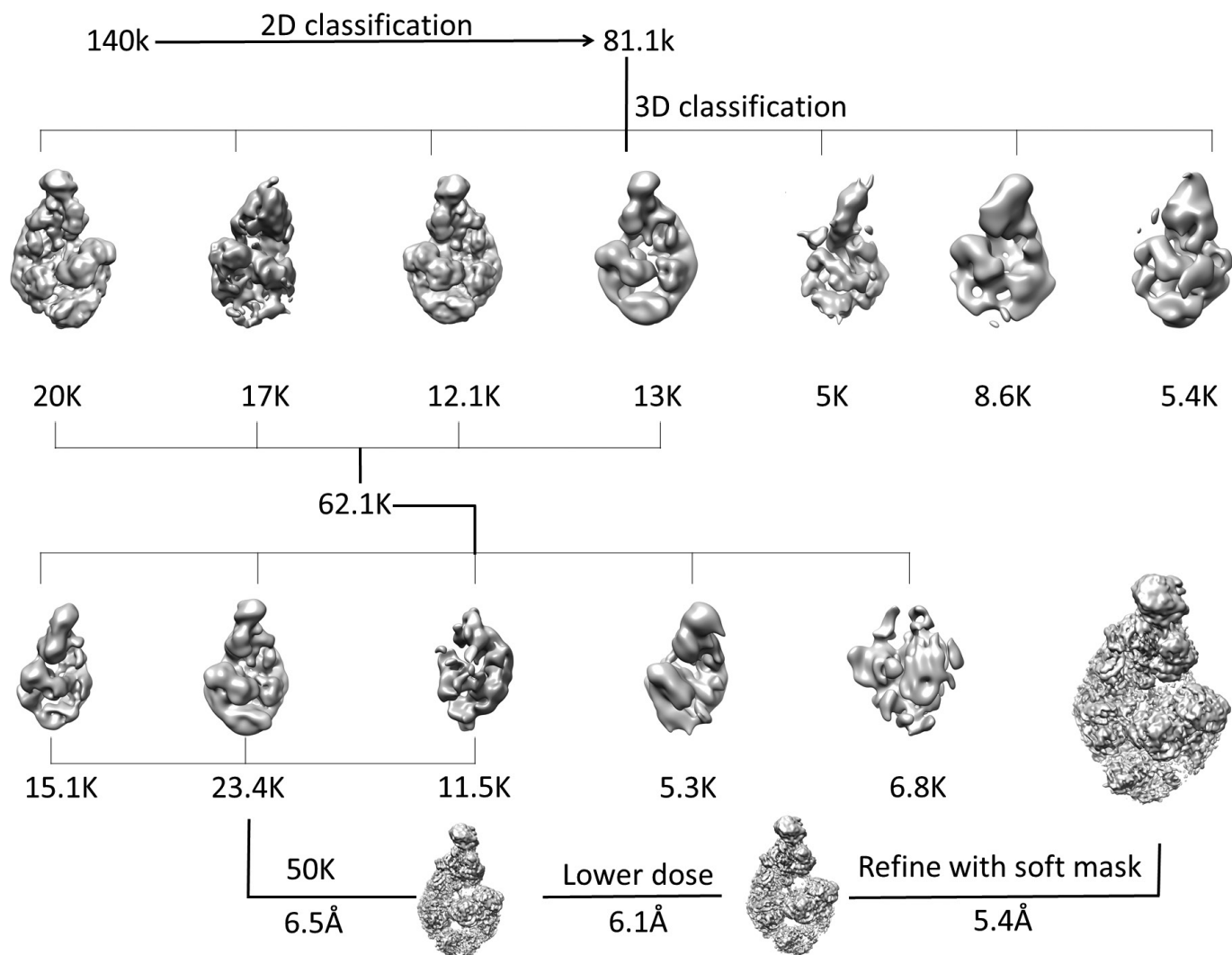


**Extended Data Figure 2 | Negative staining EM analysis of the respirasome.** **a**, A representative micrograph of negatively stained respirasomes. **b**, 2D class averages of negatively stained particles. **c**, A flowchart of the initial model generation and validation. A density

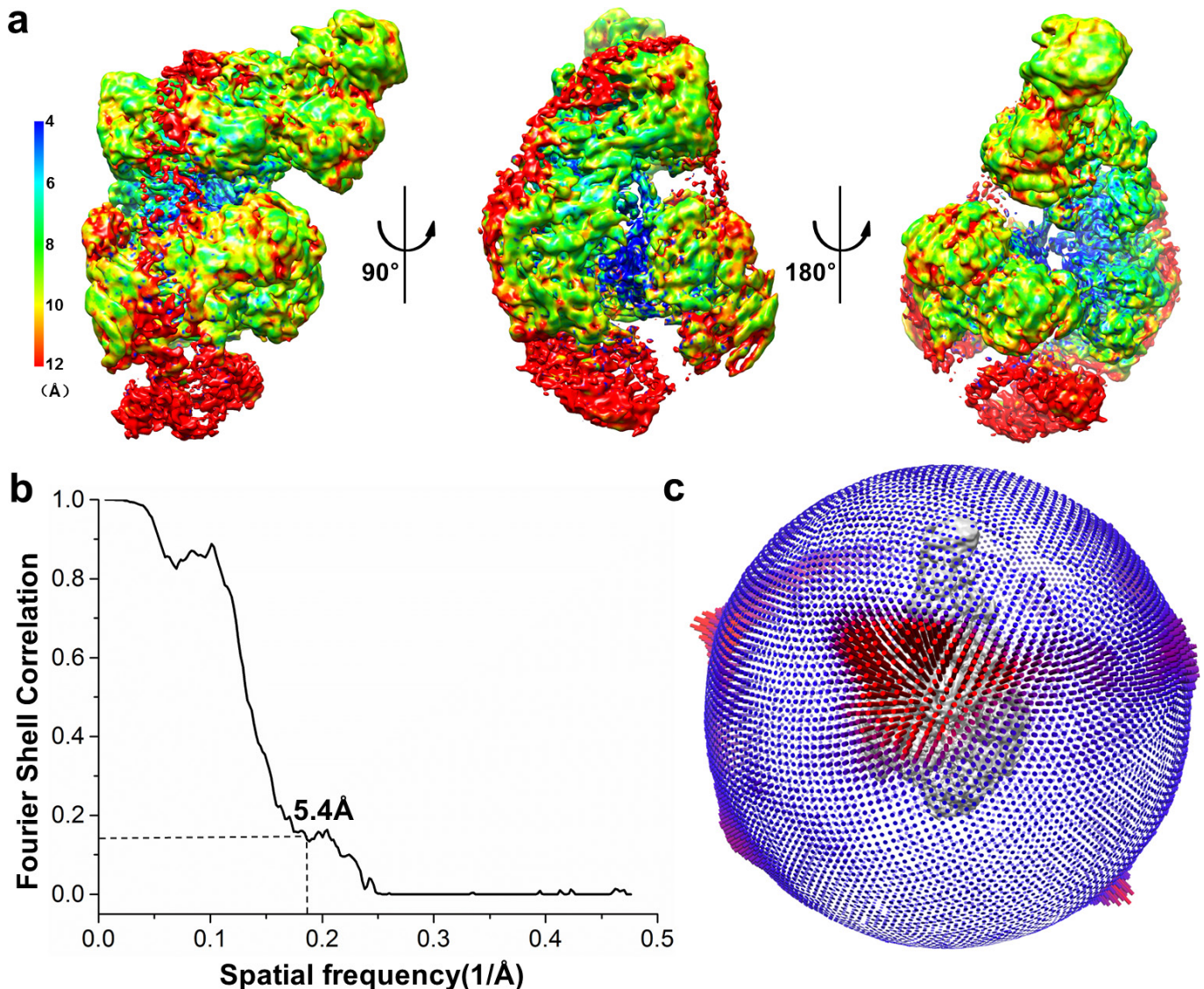
ball was used as the initial reference for 3D classification. Results of 3D classification are shown on the right, with class 1, class 2 and class 3 containing 3,031, 2,308 and 4,597 particles, respectively. Bottom left shows the final model used for the 3D refinement of cryo-EM particles.



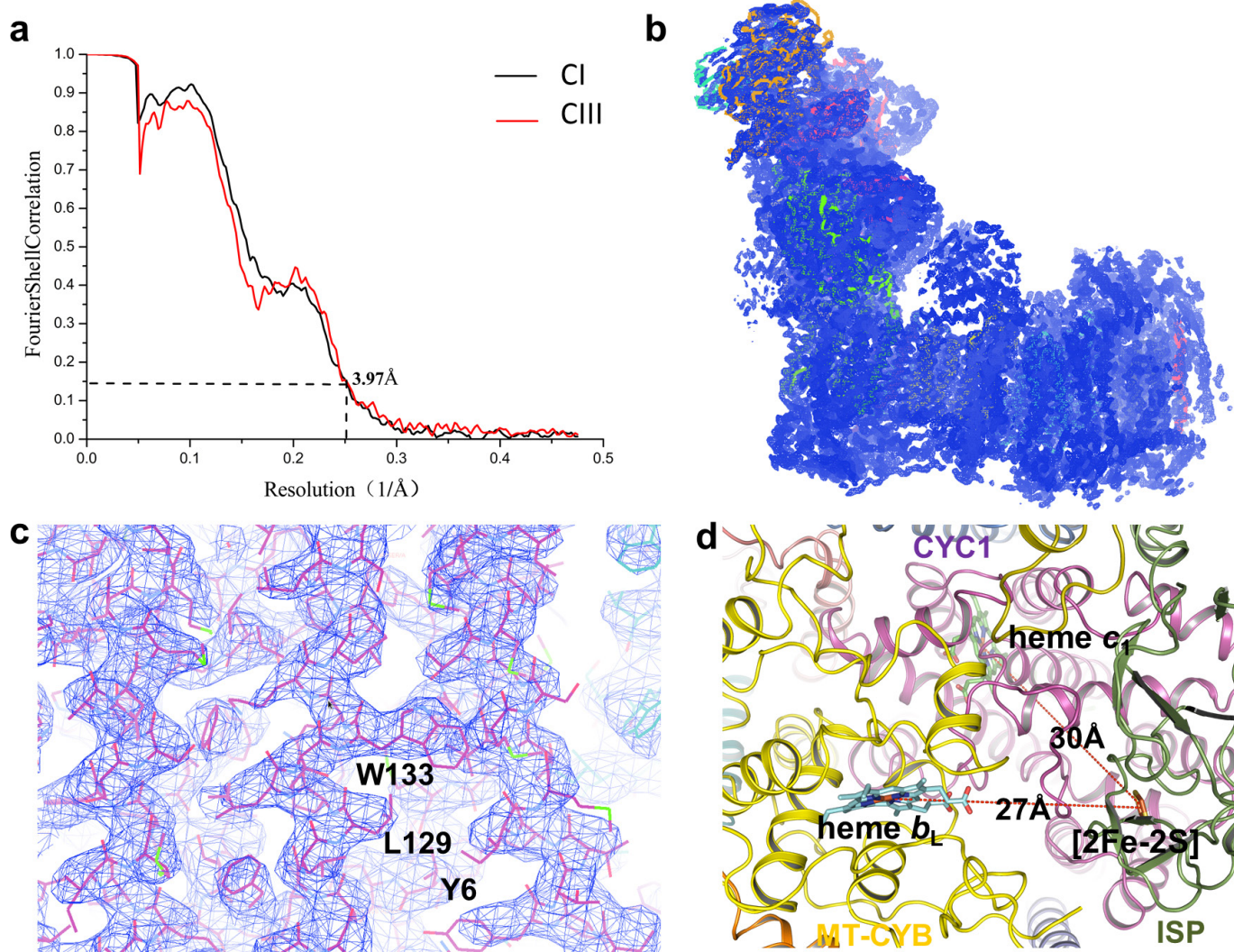
**Extended Data Figure 3 | Representative raw cryo-EM particles of the respirasome.** **a**, A representative cryo-EM micrograph of respirasome. **b**, Power-spectrum of the micrograph in **a**. The white circle indicates the  $3.0 \text{ \AA}$  frequency. **c**, A collection of raw particles of the respirasome collected with Titan Krios (300 kV) and Falcon II. **d**, Representative 2D class averages in different views.



**Extended Data Figure 4 | Workflow of 3D classification and refinement of cryo-EM particles.** Workflow of 3D reconstruction with cryo-EM data. A total of 81,100 particles were kept after 2D classification, and subject to two rounds of 3D classification. A final data set containing ~50,000 particles were used for high-resolution refinement (see Methods for more details).

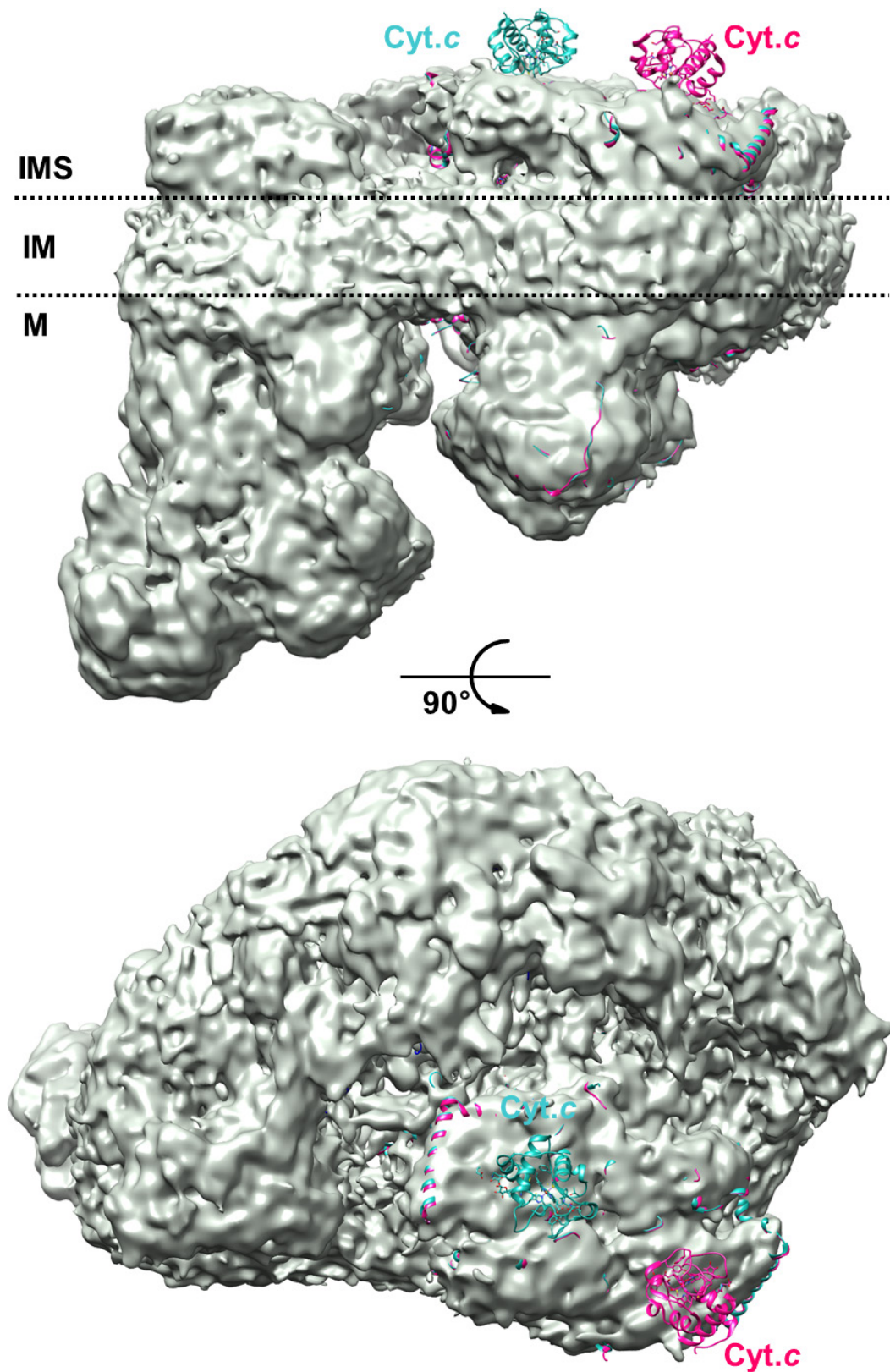


after correction of the soft-mask-induced effects. **c**, Particle orientation distributions in the last iteration of the structural refinement. Red cylinders mean more particles on these orientations. Heights of cylinders represent the relative numbers of particles.


**Extended Data Figure 6 | Structural assignment of CI and CIII.**

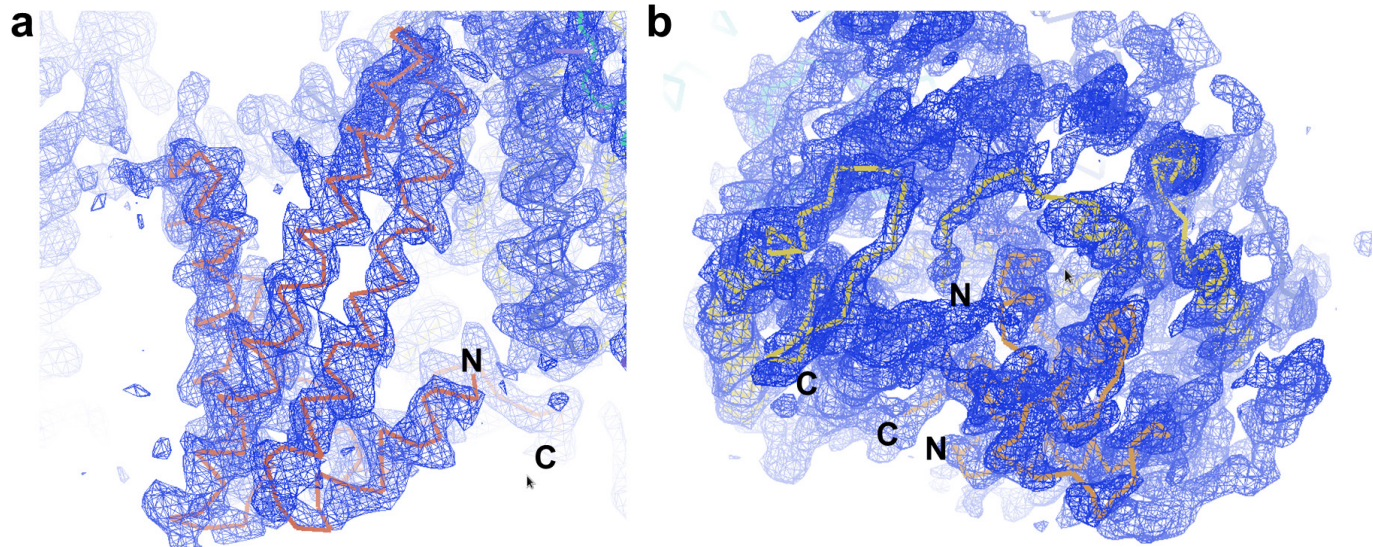
**a**, Gold-standard fourier shell Correlation (FSC) curves of the density maps of CI and CIII obtained by subregion refinement. Both the maps of CI and CIII were refined to a resolution of 3.97 Å. **b**, The density map (blue meshes) of CI is displayed at root mean squared deviation (r.m.s.d.) = 12 contour level. The backbones of core subunits are shown in the density. **c**, The density map (blue meshes) of the TM helices of ND2 is displayed at r.m.s.d. = 12 contour level to illustrate the well-resolved

side chains of ND2 at a resolution of 3.97 Å after subregion refinement. The residues are shown in line representation and three of them are labelled. The figure was prepared with Coot. **d**, CIII in our structure of the respirasome is in the intermediate state. The distances between [2Fe-2S] to haem *c*<sub>1</sub> and [2Fe-2S] to haem *b*<sub>L</sub> in the final refined CIII structure are 30 Å and 27 Å, respectively. Different subunits are coloured individually as indicated. The figure was generated using PyMOL.



**Extended Data Figure 7 | Cytochrome *c* is probably not present in the density map of the respiasome.** The expected positions of cytochrome *c* are based on the fitting of the structures of CIII with bound cytochrome *c* from yeast (PDB accession code 3CX5)<sup>67</sup>. The two cytochrome *c*

molecules of CIII are shown as blue and pink cartoons, respectively. The transmembrane region is indicated by two dashed lines. M, matrix; IM, inner membrane; IMS, intermembrane space.

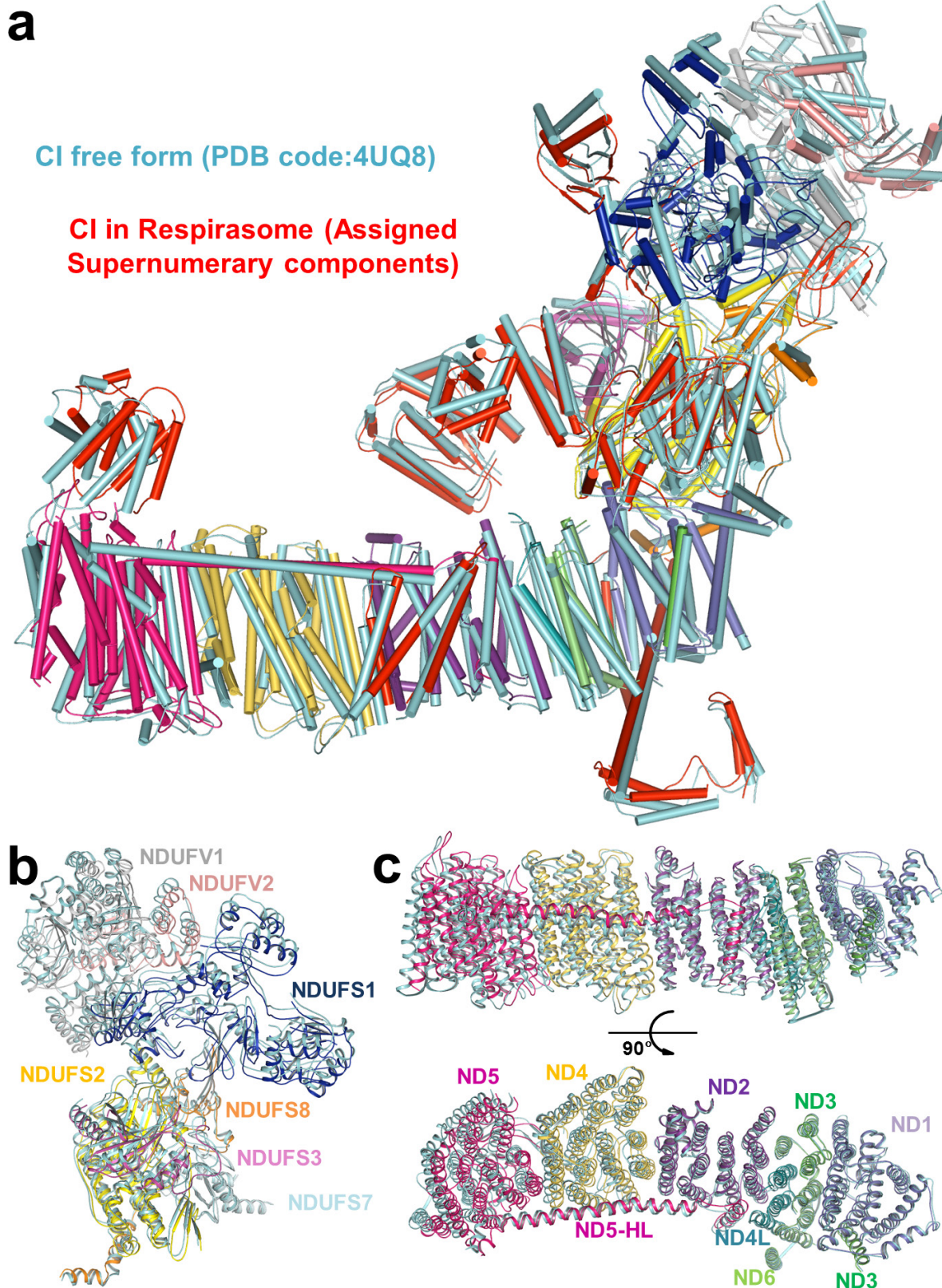


**Extended Data Figure 8 | The density map of NDUFA11, NDUFAB1 and NDUFB9.** **a**, The density map (blue meshes) of NDUFA11 is displayed at r.m.s.d. = 12 contour level. The backbone is shown in line and the N and C termini are indicated. **b**, The density map (blue meshes) of NDUFAB1

and NDUFB9 is displayed at r.m.s.d. = 12 contour level. The backbones are coloured in orange and yellow, respectively, and the N and C termini are indicated.

<b>a</b>	NDUFB9_Sus	...MAFSAPAAVLTHCQKVLRLYKFAIRHLESWCV.HRDKYRYFACIMFARFDEHKNEKDMVKATQIIRCAEEEFWYGQHP	77
	NDUFB9_Bos	...MAFLSSGAYLTHCQKVLRLYKFAIRHLESWCI.HRDKYRYFACILPARFDEHKNEKDMVKATQIIRAEAEFFWHGCHP	77
	NDUFB9_Homo	...MAFLASGPYLTHCQKVLRLYKFAIRHLESWCV.QRDKYRYFACIMPARFEEHKNEKDMAKATQIIKEAEEFFWYRCHP	77
	NDUFB9_Mus	...MAFCAPFAYLTHCQKVLRLYKFAIRHLESWCI.HRDKYRYFACIMFARFEEHKNEKDMMRATQIIRAEAEFFWQNCHP	77
	NDUFB9_Danio	...MASAYLTHSQKVLRLYKKSIRHLESWCV.YRDKYRFNACLLFAELENKEDKDMVKATMILSGEEEFFWSNCHP	73
	NDUFB9_Caenorhabditis	MESEAWMMFTKALSHRKVTBLMKRCIREVINWYGGNNLEVRFQKCIIIFARFIANACEVTRKSQIIIADGCRQLWEKRHF	80
	NDUFB9_Drosophila	...MAQVPIAVSHKRQCVSILYKFAIRNLESWYD.RRNVYRYFAVQIPLAFEDENRS.RDIEGEGIRIACGQRELFTETRF	75
	NDUFB9_Yarrowia	...MSHFVFFSAANKLIVTSMYRCSIKIARNWIS.NRQLFRQKAVEIPHKFQNAÇISNFRLIARTIDETRAHYEFRHP	76
	NDUFB9_Sus	QYIIFPESGGTSYDYEYCYKPEWCCLDWHFSEKAMYFDYFAKREQWKRLLRRESWEREVKQLQEEPTPGGPRTEALFFA	157
	NDUFB9_Bos	QYIIFPESGGTSYDYEYCYKPEWCCLDWHFSEKAMYFDYFAKREQWKKLRRESWEREVKQLQEEPTVGGRPRTEALFFA	157
	NDUFB9_Homo	QYIIFPDSEGGSYDYEYDCYKPEWCCLDWHFSEKAMYFDYFAKREQWKKLRRESWEREVKQLQEEPTPGGPRTEALFFA	157
	NDUFB9_Mus	QYIIFPDSEGGSYDYEYDCYKPEWCCLDWHFSEKAMYFDYFAKREQWKKLFMESWDREVKQLQEEPTSPDGIMTEALFFA	157
	NDUFB9_Danio	QYICFPDQGGTSYDYEYTYKPEWNWLHWHFSEKAMYFDYFAKREQWLKLAQSWEKEVQQIQSETFADGPKTEALFFA	153
	NDUFB9_Caenorhabditis	KEERFALDEGGSSYDYEYERESPDEVSDQWTIAFRECFYYFNTREQRKXELLTHWAKIEKAWDEIASIQTQLPZAAAT	160
	NDUFB9_Drosophila	QERNFEANSAGGCAFER..EVIPFLWVLDYWHFLEKAQYFYEFAKREQRKKEFVTWWEKQYKGKDPKDLGHH.....	144
	NDUFB9_Yarrowia	LEIVEPSPFGGTYKPE.....NVPPFMKIQHNIYEP.....	109
<b>b</b>	NDUFA11_Sus	RKEGDLPLPIWWHVTRPRERPM	179
	NDUFA11_Bos	RKQGDLPLPIWWHVTRPRERPM	179
	NDUFA11_Homo	RKEGDLPLPIWWHVTRPRERPM	179
	NDUFA11_Mus	RREGDLPLPIWWHVTRPRERPT	179
	NDUFA11_Danio	RKEGDLPLPIWWQFVTRPREHPI	175
	NDUFA11_Caenorhabditis	VSK.....	163
	NDUFA11_Drosophila	.....	144
	NDUFA11_Yarrowia	.....	109
	NDUFA11_Sus	.MAKITLLHKSDIPEGTECHFKAYASTSIGGAIGLIVSAYS.IAIKPFAASFLEGVARTGRYTFSTAAGIAIFGLITSCIS	77
	NDUFA11_Bos	.MAKITVLRCYWDIPEGTECHRKTYATTISIGGAAGLVVSAYS.VAIKTPFISFLEGVARTGRYTFSTAAGIAIFGLITSCIS	77
	NDUFA11_Homo	.MAPKVFRCYWDIPEGTECHRKAYSTTSIASVAGLTAAAYR.VTINPCTFLEGVAKVGQYTFSTAAGIAIFGLITTCIS	77
	NDUFA11_Mus	MAMAKRFFESYNEVPDGTQCHFKTYITTAIGGIGIIGSAYS.VTINPCTFLEGVAKVGQYTFSTAAGIAIFGLITTCVS	79
	NDUFA11_Danio	.....MCYWDLIEEGKDCVAKTVTTKVALTVGLVATAYR.MVIFKPEPFICALTSAASITGTMAMGAIFGMMTCIS	71
	NDUFA11_Drosophila	.....MSIILRSKYDHDGDAFGKIVATNKYAVSAGVSMFCVLTISKPCGYLFTLGFRAFYNTGPEIMGMATAFILITIVA	77
	NDUFA11_Yarrowia	.....MIRQSVLRLSRAAVAREPLSRSFVTAVAREQLVRAAFVSEIRHYSSAHVITKDMIQERIVAILLESFDK	68
	NDUFA11_Sus	AÇVREKPKDDFLNYFIGGCAGGITLIGARTRSYGIACAAACAYMLTAALVKMGQLEGWQVFAEKV.....	141
	NDUFA11_Bos	AÇVREKPKDDFLNYLIGGCAGGITLIGARTRSYGIACAAACAYMLTAALVKMGQLEGWQVFAEKV.....	141
	NDUFA11_Homo	AHREKPKDDFLNYFIGGCAGGITLIGARTHNYGIGAAACAVYFCIAASIVKMGRLLEGWVEVFAEKV.....	141
	NDUFA11_Mus	AQVREKPKDDFLNYFIGNCAGGITLIGVRTHSYGTAAMGCVYMGTAALFKIGKLEGWEIPTKSSN.....	145
	NDUFA11_Danio	AÇIRDEPDSFANYFIGGCASGVFLGARTHSPMTCTMACVGICLTVAMILTKVGKMEGWKTIKSEKI.....	135
	NDUFA11_Drosophila	TNARGKIDKINYIIGGFAAGGVFGAWKHNHVACLCAGIFLICIAQVIKMSIECGWEFFNPPIKQYGGINIAGNDWTIM	156
	NDUFA11_Yarrowia	VNDAKNITATANITSIDLGLSIDVVVEVVMAIEFFGLEIPDHDAEIKTVQQAIDYVSAQFAAV.....	132
<b>c</b>	UQCRC1_Sus	FSSLSCTYVETAVIAFTP 267	
	UQCRC1_Bos	FSLCLSGTYDEIAVETIISP 267	
	UQCRC1_Homo	IGCIWWTYAEELAVFTLTP 267	
	UQCRC1_Mus	ISSVSFVYEEFLAVFGLTIP 267	
	UQCRC1_Danio	IGCCISFYEGLAVEVILP 261	
	UQCRC1_Drosophila	IQRLEAS...ILPFEITIP 257	
	UQCRC1_Caenorhabditis	FGEKLKH...ISSTIEFP 246	
	UQCRC1_Yarrowia	FSHLFSS...QSFVELGTP 248	

**Extended Data Figure 9 | Sequence alignments of NDUFB9, NDUFA11 and UQCRC1 from different species . a.** Sequence alignment of the NDUFB9 subunit of CI from different species. **b.** Sequence alignment of the NDUFA11 subunit of CI from different species. **c.** Sequence alignment of the UQCRC1 binding motif from different species. All alignments were carried out using DNAMAN.



**Extended Data Figure 10 | Conformational change of CI.** **a**, Conformational changes of the core and assigned supernumerary subunits of CI. The model of CI in the respirasome (with subunits individually coloured) is globally aligned to the model of free CI (PDB accession code 4UQ8) (coloured in cyan). **b**, Comparison of the seven matrix core subunits of CI

in the free form and in the respirasome. The polypeptides are indicated in different colours and labelled with text in the same colour. **c**, Same as **b**, but indicating the comparison of the seven membrane-bound core subunits. The bottom panel is viewed from the matrix side.